Numerical Simulation of a Shock Tube in Thermochemical Non-Equilibrium

Justin Clarke*, Alex Glenn †, Matthew McGilvray ‡, Luca di Mare §
University of Oxford, Oxford, Oxfordshire, OX1 2JD

An efficient method is developed for calculating the non-equilibrium properties of the test gas in a shock tube in the shock frame of reference. The one dimensional method is based on the parabolised Navier-Stokes equations, resulting in a form similar to a stagnation line problem but with appropriate consideration of the mass loss to the boundary layer present in a shock tube. Gas properties are determined using Park's two temperature model. Transport properties are evaluated using second order Chapman-Enskog theory. The centreline solution is coupled to an artificial radial pressure profile which mimics the effect of a boundary layer. The method was tested on a variety of air cases ranging from 5.5 km/s to 9.6km/s, and demonstrated improved modelling of the non-equilibrium regions compared to a Rankine-Hugoniot solver. A 6.1 km/s, 13.3 Pa test case relevant for Titan entry demonstrates the necessity of appropriately modelling mass loss to the boundary layer in a shock tube. The effect of shock structure and mass loss to the boundary layer in a non-equilibrium flow within a shock tunnel is shown to substantially impact the test gas properties and non-equilibrium radiance profiles in the UV/Vis and Vis/IR regions.

I. Nomenclature

A^*_{ij}	=	ratio of collision integrals for an interaction between species i & j
b	=	non-dimensional impact parameter
B^*_{ij}	=	ratio of collision integrals for an interaction between species i & j
$C_{p,i}$	=	molar specific heat for species i
$\hat{D}_i$	=	average vibrational energy per unit mass of species i removed or added to a gas mixture
D_{ij}	=	multicomponent diffusion coefficient
e	=	electron charge
$e_{v,i}$	=	vibrational energy of species i
e_V	=	vibrational-electronic energy of gas mixture
h	=	gas mixture enthalpy
h^0	=	total enthalpy
$h_{i,V}$	=	vibrational-electronic enthalpy of species i
$\hat{I}_i$	=	first ionization energy of species i
k_B	=	Boltzmann's constant
$k_{b,r}$	=	backwards reactant rate coefficient for reaction r
$k_{f,r}$	=	forwards reactant rate coefficient for reaction r
M_i	=	molar mass of species i
n_e	=	electron number density
$\dot{n}_{ei}$	=	molar rate of production per unit volume of species i due to electron impact ionization
NJ	=	total number of species and catalytic bodies in the gas mixture
NR	=	number of reactions considered in the gas mixture
NSP	=	number of species in gas mixture
p	=	pressure

*DPhil Candidate, Oxford Thermofluids Institute, Department of Engineering Sciences.
†DPhil Candidate, Oxford Thermofluids Institute, Department of Engineering Sciences.
‡Associate Professor, Oxford Thermofluids Institute, Department of Engineering Sciences.
§Associate Professor, Oxford Thermofluids Institute, Department of Engineering Sciences.

P_e = electron pressure
$\mathbf{q}$ = vector of state variables
q_k = kth component of the heat flux vector
$\mathbf{r}$ = vector field of the cylindrical coordinate system
r = radial coordinate in the cylindrical coordinate system
R = universal gas constant
$\bar{R}$ = specific gas constant
r' = radius
r_c = non-dimensional radius
$R_{b,r}$ = backwards reactant rate for reaction r
$R_{f,r}$ = forwards reactant rate for reaction r
T = translational-rotational temperature
T^* = non-dimensional temperature
T_{av} = Two-Temperature model average temperature
T_e = electron temperature
T_{el} = electronic temperature
T_v = vibrational temperature
u_r = velocity component in the r direction
u_θ = velocity component in the θ direction
u_z = velocity component in the z direction
$\mathbf{V}_i$ = diffusion velocity vector for species i
$\dot{w}_i$ = mass rate production of species i
$\mathbf{x}$ = vector of mole fractions
X_i = molar concentration of species i
$\alpha_{i,r}$ = stoichiometric coefficient of reactant i in reaction r
$\beta_{i,r}$ = stoichiometric coefficient of reactant i in reaction r
η = viscosity
λ = total thermal conductivity
λ_{tr} = translational thermal conductivity
λ_{rot} = rotational thermal conductivity
λ_v = vibrational thermal conductivity
λ_e = electron thermal conductivity
λ_{el} = electronic thermal conductivity
ν_{ei} = effective collision frequency for electrons and species i
ρ = density
ρ_i = density of species i
σ = radius corresponding to the minimum of the intermolecular potential
$< \tau_i >$ = tranlational-vibrational energy relaxation time for species i
θ = angular coordinate in the cylindrical coordinate system

II. Introduction

Non-equilibrium phenomena alter the heat transfer and aerodynamic characteristics of vehicles entering planetary atmospheres. The design of vehicles entering planetary atmospheres relies heavily on numerical calculations, and in turn these require accurate estimates of physical quantities such as rate constants and intra-molecular interaction parameters. Rate constants and intra-molecular parameters for transport quantities used in numerical predictions of hypersonic flows draw information from a broad range of sources [1]. However, the flow conditions typical of planetary entry are unattainable in continuous flow facilities and must be studied using shock tube facilities.

Shock tube facilities comprise several compression stages using shock heating processes to generate the required flow [2]. The processes taking place in a shock tube determine the history and spatial variation of the properties of the test gas, as such characterization of the test gas state in a shock tube is not a trivial exercise, requiring stipulations about the condition of the test gas when analysing spectroscopy data from shock tubes. As an example, determining rate coefficients for high-temperature reactions from spectroscopic data generated by shock tubes [3–6] requires assumptions about temperature and pressure of the test gas. When radiation measured in shock tubes is used, it is commonly assumed

that the test gas has a uniform temperature profile corresponding to the nominal shock speed just upstream of the optical measurement station. Park attempted to account for boundary layer effects by assuming a linear increase of density and temperature behind the shock [7]. However, recent results have shown the importance of shock trajectory on the temperature profile of the test gas, and its influence on the prediction of radiation spectra for equilibrium conditions [8]. It has been shown that the flow is in a state of thermal and chemical non-equilibrium in many tests performed in high-speed expansion tube experiments [9]. Common strategies for modelling thermochemical non-equilibrium are to use a two (or more) temperature models such that the temperatures for energy modes are considered separately [10–12]. A set of chosen reactions with specified equations for calculation of the forward and backward reaction rates allows modelling of the chemical non-equilibrium [1, 13]. Consideration of relaxation between energy modes and various forms of diffusion can be accounted for through additional parameters [14].

This paper introduces a new method to account for the effect of both shock structure and non-equilibrium phenomena on spectroscopy data in shock tube experiments. The low computational cost of the method provides an ideal platform for optimisation of parameters such as reaction rates used in thermochemical modelling. The method is demonstrated for experiments in synthetic air and a nitrogen-methane mixture relevant for Titan entry using Park's two temperature model and second-order approximation Chapman-Enskog transport properties.

III. Non-Equilibrium Shock Solver (NESS)

The need for appropriate consideration of the fluid dynamics relevant to shock tubes has been highlighted by recent work. Satchell et al. [8, 15, 16] and Collen et al. [17] highlighted the importance of the combined consideration of boundary layer effects and shock speed variation. Clarke et al. [18, 19] highlighted the importance of consideration of the boundary layer for non-equilibrium flows as well as the importance of resolving shock structure. Additionally, questions arising from the discrepancy between experiments relevant to low Earth orbit return and equilibrium modelling have raised questions regarding the effect of radiance produced and absorbed within the boundary layer [12]. These works, combined with the need to be computationally lightweight for parameter optimisation, highlight the need for a solver which can appropriately model:

1) Shock structure
2) Thermochemical non-equilibrium
3) Mass loss to the boundary layer
4) Boundary layer compression of the core flow
5) Radiance from the boundary layer
6) Shock speed variation

The Non-Equilibrium Shock Solver (NESS) is a computationally low-cost method which resolves shock structure, thermochemical non-equilibrium, mass loss to the boundary layer and boundary layer compression. The NESS algorithm implements the following numerical method for a chosen fill composition and thermochemistry regime, and requires inputs of shock speed, tube diameter and fill temperature, pressure and composition.

The flow in the shock tube is assumed axisymmetric and steady (i.e. constant shock speed), and can be described in cylindrical coordinates by the two-dimensional, two-temperature Navier-Stokes equations in conservation form (adapted from [14]). Since the centreline is a streamline, the parabolised Navier-Stokes equations can be treated by separation of variables. This models the flow in the shock tube as a one-dimensional steady flow in a compressible medium, which assumes the contact discontinuity is travelling at the shock velocity [20]. The length of the test slug is denoted as δ, and is taken as L_m using the Mirels estimate for fully developed shock tube flow [21]. The x direction is the longitudinal direction of the shock tube while r is the radial direction (see Figure 1).

Further simplifications can be made by accounting for the symmetry conditions around the centreline itself, which require scalar variables and the radial velocity to have a gradient of zero. Symmetry and separation of variables allow the parabolised Navier-Stokes equations to be written as a set of coupled one-dimensional equations by expanding the solution near the centreline with respect to a small parameter, which represents the distance from the centreline itself.

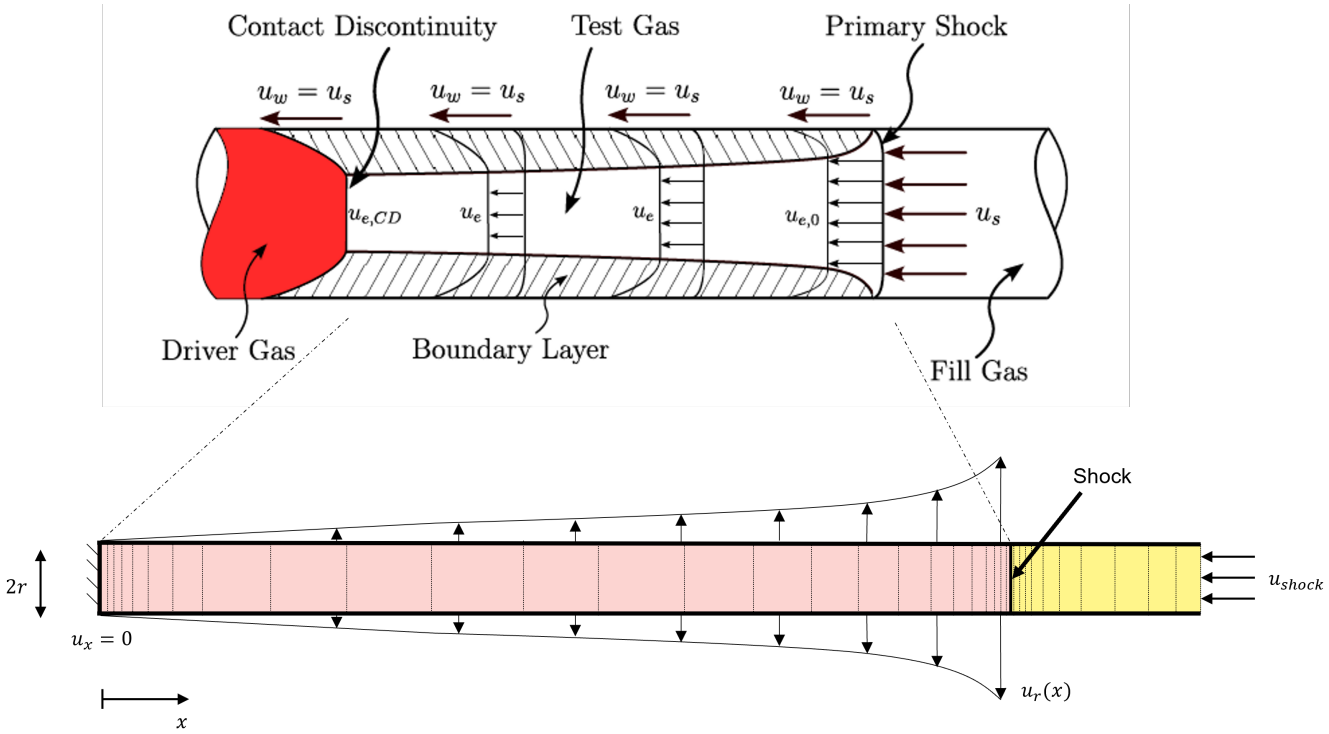

Fig. 1 Diagram illustrating the formulation of NESS and region of applicability to a shock tube.

This allows the state and flow variables to be written as:

$$\begin{aligned}
\frac{\partial}{\partial\theta} &= 0 \\
u_\theta &= 0 \\
u_r &= u(x) \\
u_x &= v(x) \\
p &= p_0(x) + p_1(x)r \\
T &= T(x) \\
T_v &= T_v(x)
\end{aligned}$$

Substituting into the Navier-Stokes equations and simplifying results in the equations 1-5, allowing the test slug equations to be formally similar to the equations ruling stagnation line problems.

$$\frac{\partial}{\partial x}\rho v + \frac{\rho u}{r} = 0 \tag{1}$$

$$\frac{\rho u^2}{r} + \frac{\partial}{\partial x}\rho uv = -p_1 + \mu\left(\frac{\partial^2 u}{\partial x^2} - \frac{4u}{3r^2}\right) \tag{2}$$

$$\frac{\partial}{\partial x}\rho v^2 = -\frac{\partial}{\partial x}p + \mu\left(\frac{4}{3}\frac{\partial^2 v}{\partial x^2} + \frac{u}{3r}\frac{\partial u}{\partial x}\right) \tag{3}$$

$$\frac{\partial}{\partial x}\rho v h^1 + \frac{\rho u h^1}{r} = -\frac{\partial}{\partial x}q_x + \mu\left(\frac{4}{3}\left(\left(\frac{\partial v}{\partial x}\right)^2 - \frac{u}{r}\frac{\partial v}{\partial x} + \frac{u^2}{r^2}\right) + \left(\frac{\partial u}{\partial x}\right)^2\right) \tag{4}$$

$$\frac{\partial}{\partial x}\rho v e_V + \frac{\rho u e_V}{r} = -P_e\left(\frac{\partial v}{\partial x} + \frac{u}{r}\right) - \frac{\partial}{\partial x}x q_{x,v} + \frac{\partial}{\partial x}g_x + \psi \tag{5}$$

Where:

$$
\begin{aligned}
h^1 &= h + 1/2(u^2 + v^2) \\
q_x &= -(\lambda_{tr} + \lambda_{rot})\frac{\partial T}{\partial x} && (6)\\
q_{x,v} &= -(\lambda_v + \lambda_{el} + \lambda_e)\frac{\partial T_v}{\partial x} && (7)\\
g_x &= \sum_{i=1}^{NSP} h_{i,V}\mathbf{V}_i^x && (8)\\
\psi &= \sum_{i=1}^{NSP} \rho_i \frac{e_{v,i}(T) - e_{v,i}(T_v)}{<\tau_i>} + 2\rho_e \frac{3}{2}\bar{R}(T - T_v)\sum_{i=2}^{NSP}\frac{\nu_{ei}}{M_i} && (9)\\
&\quad - \sum_{i\neq\text{charged}}^{NSP} \dot{n}_{ei}\hat{I}_i + \sum_{i=1}^{NSP}\dot{w}_i\hat{D}_i && (10)
\end{aligned}
$$

The effect of an artificial boundary layer can be examined by specifying a function for $p_1(x)$, which will be taken as the Mirels' estimate for the radial velocity. This scales the radial velocity with the the inverse of the square root of the post shock distance such that $u \propto 1 - \sqrt{1 - x/\delta}$. The radial velocity at the edge of the boundary layer determines, in turn, the test time which is computed as part of the solution. The flow equations, closed by the thermochemistry model equations, are discretised using a second order accurate finite volume method and cast as a large system of coupled algebraic equations. Experimental shock velocity, fill pressure and temperature, and the Mirels' estimate of the slug length allow the system of equations to be cast as a boundary value problem. The system is solved using Newton iterations based on exact Jacobian matrices, with the grid refined recursively such that the shock is fully resolved. Appropriate resolution is met when all solution variables are within 0.1% of the results from the previous iteration, grid points are added where this metric is not met. This allows regions of large gradients to have high mesh density and enforces mesh convergence of the final solution.

IV. Thermochemical Model

When chemical reactions in a gas mixture proceed at finite rates, the conservation of energy and mass equations for each species require rate-of-production terms for chemical species. For a multi-component gas, the stoichiometric relations for reactants and products with NSP chemical species and $r \in$ NR number of reactions considered are [22]

$$\sum_{i=1}^{NJ}\alpha_{i,r}X_i \underset{k_{b,r}}{\overset{k_{f,r}}{\rightleftharpoons}} \sum_{i=1}^{NJ}\beta_{i,r}X_i \tag{11}$$

With NJ equal to the number of species NSP plus the number of catalytic bodies. $\alpha_{i,r}$ and $\beta_{i,r}$ are the stoichiometric coefficients of the reactants and products respectively, and $k_{f,r}$ and $k_{b,r}$ are the forward and backwards reactant rate coefficients for the rth reaction respectively. X_i is the molar concentration in moles/unit volume. Moss showed that the net mass rate of production $\dot{w}_i$ of the ith species per unit volume is obtained by [23]

$$\dot{w}_i = M_i\sum_{i=1}^{NR}(\beta_{i,r} - \alpha_{i,r})(R_{f,r} - R_{b,r}) \tag{12}$$

where $R_{f,r}$ and $R_{b,r}$ are the forward and backward reaction rates respectively, defined by

$$R_{f,r} = \left[k_{f,r}\prod_{i=1}^{NSP}(\rho_i/M_i)^{\alpha_{i,r})}\right] \tag{13}$$

$$R_{b,r} = \left[k_{b,r}\prod_{i=1}^{NSP}(\rho_i/M_i)^{\beta_{i,r})}\right] \tag{14}$$

The thermodynamic model considers thermal and chemical non-equilibrium according to Park's two temperature model [1]. The two-temperature model assumes the rotational and translational temperature of the heavy particles are

matched at temperature T. The model also assumes that the vibrational temperature of the molecules, the translational temperature of the electrons, and electronic excitation of the atoms and molecules are matched at temperature T_v. This assumption is based on the very fast transfer of energy between the vibrational motion of N_2 and the translational motion of free electrons [24, 25], and the low-lying electronic states of the species equilibriate quickly with the ground electronic states [24]. The dissociation rate coefficients $k_{f,r}$ are assumed to be functions of the geometric mean of the two temperatures

$$T_{av} = \sqrt{TT_v} \tag{15}$$

while $k_{b,r}$ is a function of only translational temperature [22]. The reactions, reaction rate equations and reaction rates can be chosen depending on the problem considered. The blended Millikan-White [26] and Park approximation [27] used in [14] for the vibrational-translational energy relaxation is used, while transport properties have been determined by using second order Chapman-Enskog approximations using methods and coefficients described in [22].

V. Validation

To validate the Non-Equilibrium Shock Solver (NESS) algorithm, the 11-species air model using reaction rates from Dunn and Kang [28] and relaxation parameters from [14] was used with the artificial radial pressure function $p_1(x)$ set to zero. Various validation activities were performed to determine the performance of NESS in matching shock structure and thermochemistry models. These are detailed below, and demonstrate the algorithms applicability to shock tube problems.

A. Shock Structure

A Mach 2 shock propagating through air with constant thermodynamic properties and a Prandtl number of $3/4$ has an analytical solution found by Morduchow and Libby [29]. Figure 2 show the pressure and velocity ratios of NESS with the analytical model, with the shock centred about zero. The velocity distribution is accurate to within 3% and the pressure distribution is within 8%. Given the small distance scale of these results, the modelling of viscous effects and the subsequent effect on shock structure produces a satisfactory match. This also indicates the code is producing a sufficiently fine mesh to appropriately resolve shock structure and is converging to a resolved result.

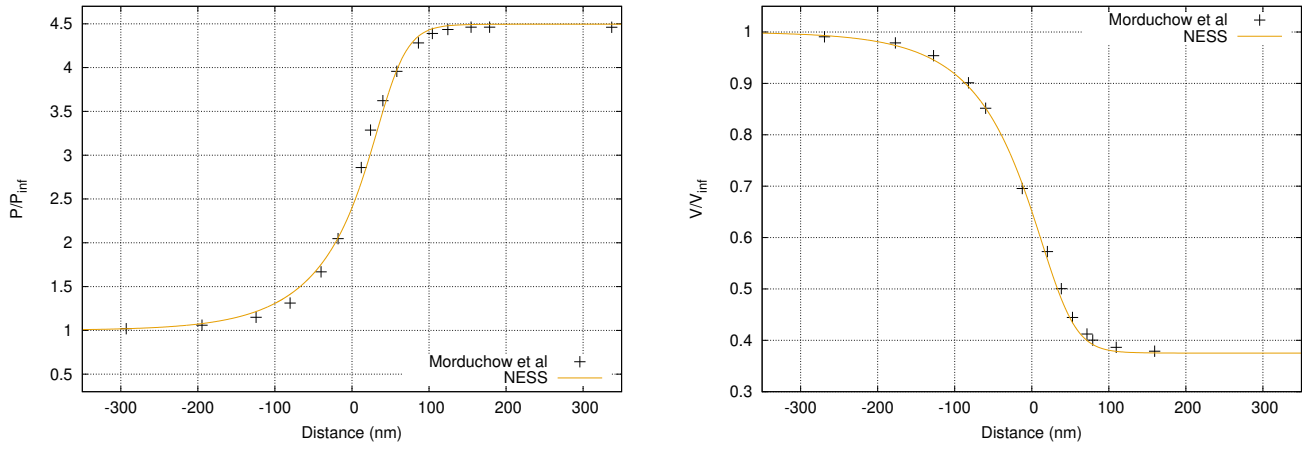

Fig. 2 Mach 2 shock structure of: (a) the pressure ratio P/P_∞ and (b) the velocity ratio v/v_∞.

B. Thermochemistry

Thermochemistry and transport property modelling in NESS follows the methodology of [14]. The transport properties utilised by NESS are calculated using the polynomial fits found in Gupta et al., therefore direct comparisons could be made to example calculations from [22]. Similarly, verification of appropriate calculation of rate coefficients could be conducted by direct comparison to of calculations in [14].

The performance of the combined shock and thermochemistry model was validated by comparison to the University of Queensland's POSHAX3 algorithm [30], which is a one-dimensional code utilising spatial marching to apply a chemical relaxation scheme behind a frozen post shock state. The validation case used is a comparison case developed by Gollan [31] comparing the kinetic schemes of Marrone et al. [32] and Gupta et al. [22]. The case chosen is a Mach 12.28 shock in synthetic air at 300 K and 133.32 Pa, using a single temperature model. The comparisons between NESS, POSHAX3 and Marrone et al. are shown in Figure 3, with NESS comparable with the POSHAX3 data to within 2% for major species. This is expected, as the same kinetic reaction scheme from Gupta et al. is used. Differences are found closer to the shock due to NESS fully resolving the shock structure, using the definition of shock location as the location of peak temperature. POSHAX3 relaxes the gas from a frozen post shock state, whereas reactions will have proceeded in NESS across the shock during the increase in temperature and pressure due to the resolution of the shock structure. By approximately 0.02mm behind the shock, the reactions have proceeded to comparable points. If strongly radiating species are produced in this region, the high temperatures could result in significant radiance increases.

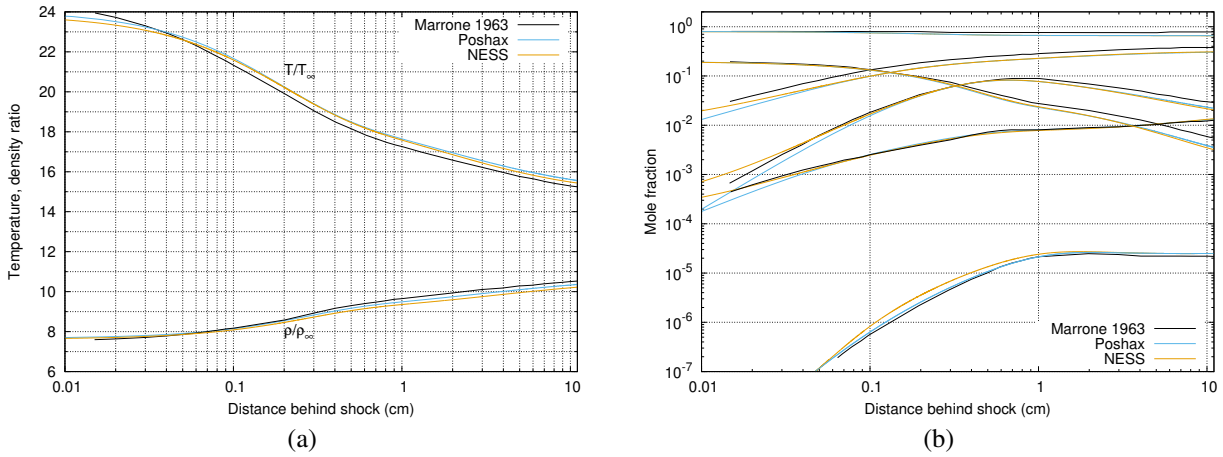

(a) (b)

Fig. 3 Validation of NESS against POSHAX3 and results from Marrone et al. for a Mach 12.28 shock. a) Temperature and density distribution and (b) Mole concentrations.

VI. Results

A variety of test cases will be considered to analyse the performance of NESS, utilising spectroscopy comparisons between experimental results and those generated numerically. In the experiments, radiance is imaged axially onto spectrometers, allowing spectral and spatial resolution. The cases are taken from two experimental shock tunnels, the University of Oxford's T6 Stalker Tunnel and the NASA-EAST electric arc driven tunnel.

The University of Oxford T6 Stalker Tunnel is a multi-mode shock tube utilising a free-piston driver to perform hypervelocity experiments. The mode of operation in the experiments considered from T6 was the aluminium shock tube (AST) mode, which has been extensively described [33, 34]. The AST has a conical expansion from 96.3 to 225mm after the secondary driver (see Figure 4), with 6m separating the end of the conical expansion to the viewing window of the spectroscopy equipment.

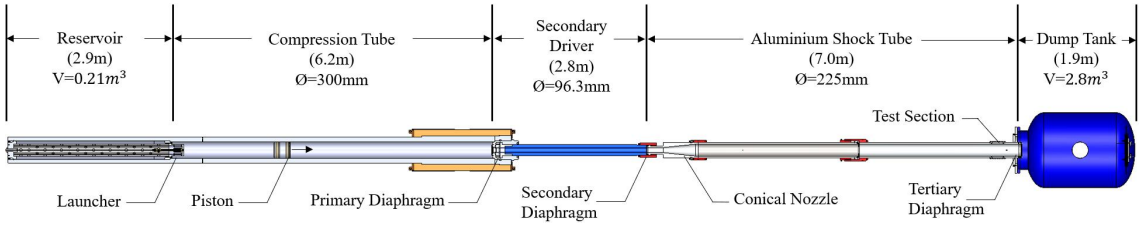

Fig. 4 Section view of the T6 shock tunnel in AST mode. Image from [12].

The NASA Electric Arc Shock Tube (EAST) has been described comprehensively by Cruden [35] and will only be briefly described. A 101.6mm diameter aluminium shock tube is coupled with an electric arc driver and dump tank. A 125mm viewing window with spectroscopy units is located at approximately 7.5m downstream.

Both tunnels generate a shock driven by the rupture of a primary diaphragm due to a build up of high temperature and pressure gas, generating high enthalpy flows allowing ground testing to be conducted on hypersonic flows.

The high speed flows generated in these facilities can be analysed through numerical models such as NESS, these numerical models require coupling with a radiance solver. NASA's NEQAIR v15.1 [36] was used to determine the radiance outputs from the specified temperatures and number densities from the numerical model. An approximate spatial resolution function (SRF) and instrument line shape (ILS) convolves the NEQAIR simuluations to account for broadening mechanisms contained within the experimental setup, enabling comparison between the experimental and numerical results.

Section III referenced the importance of consideration of the shock trajectory. Satchell et al. and Collen et al. demonstrated the importance of shock trajectory on the temperature profile of the test gas, and its influence on the prediction of radiation spectra for equilibrium conditions [8, 15–17]. Satchell et al. developed a method (utilised in the LASTA code) which considered the shock history effect by elevating Lagrangian slices to their respective post-shock states as the shock propagates down the tube. The entropy of the shocked Lagrangian is then assumed to remain constant. Each Lagrangian slice evolves at constant enthalpy and entropy under the action of sound waves propagating along the test slug. Mirels' boundary layer effects are also considered, further accounting for flow non-uniformities. LASTA results are shown when shock trajectories are known, giving an indication of shock history effects on the equilibrium radiance levels.

The first test case considered in this paper are two shots relevant for Earth return missions in 79% N_2, 21% O_2 by volume fill gas taken from the work of Collen [33]. The shock speed and fill pressure considered is 9.54 km/s through 13.3 Pa fill gas. The spectral region of interest is the oxygen 777nm triplet.

The second group of test cases considered in this paper were gathered during a campaign using the T6 tunnel in aluminium shock tube (AST) mode, designed to examine radiation experienced during the descent of vehicles from Low-Earth Orbit [12]. Test cases ranging from 5.5-7.1 km/s at a nominal post-shock pressure of 1 bar in synthetic air (20.78% O_2 and 79.22% N_2 by volume) produced radiance data in the UV/Vis and Vis/NIR spectral ranges.

The third group of test cases compares one shot from the LEO orbit return campaign of Glenn et al. to a comparable experiment from NASA-EAST. Using synthetic air (20.78% O_2 and 79.22% N_2 by volume), the two cases are for shock speeds and fill pressures of 6.64 km/s, 106.7 Pa for the T6 shot and 6.81 km/s, 94.13 Pa for the EAST case. Radiance data is compared in the UV/Vis and Vis/NIR spectral ranges.

Finally, the last test case considered is taken from Brandis and Cruden and is 6.1 km/s shock travelling through 13.3 Pa, 2% CH_4 and 98% N_2 by volume fill gas [37]. This gas composition is relevant for Titan entry, which generates significant radiance due to the presence of CN and C_2 [37].

To find the relevant slug length, the tube diameter, fill gas composition and shock speed are used as inputs to the equation for maximal test slug length developed by Mirels [20]. This further reduces the required inputs of the code to measurable quantities.

The thermochemistry model for synthetic air cases uses forward reaction rates and Millikan-White constants from Park [13], with equilibrium constants calculated from Gnoffo et al. and supplemented with polynomial fits from Kim [38]. Ambipolar diffusion and energy loss due to electron impact ionization are modelled using parameters from Gnoffo et al. [14].

The thermochemistry model for the Titan entry case uses forward reaction rates from Gökçen, with equilibrium constants calculated from NASA polynomial fits for thermodynamic properties [39]. Ambipolar diffusion and energy loss due to electron impact ionization are modelled using parameters from Gnoffo et al. where relevant [14]. Transport properties are modelled using nitrogen based collision integrals from Gupta et al. [22], as the additional carbon-containing species alter the viscosity by less than 5% up to 30000 K and the thermal conductivity by less than 10% for temperatures lower than 13000 K [40].

All simulations using NESS were completed using a personal computer with single threading, and took less than 4 minutes per run.

A. T6 Tunnel Experiment for Earth Return

The first test case considered in this paper is relevant for Earth return missions, taken from Collen [33]. We consider shot T6s164, a 9.59 km/s shock through 13.3 Pa, 300K in 79% N_2, 21% O_2 by volume fill gas to compare three functions

for $p_1(x)$, $p_1 = 0$, $p_1 \propto x/\delta$, and $p_1 \propto 1 - \sqrt{1 - x/\delta}$ for $x < \delta$ where δ=468 mm is the maximal test slug length. This corresponds to an assumption of a Rankine-Hugoniot model, blunt body sphere model or a Mirels shock tube model [21] for the respective radial velocity profile, visualized in Figure 5.

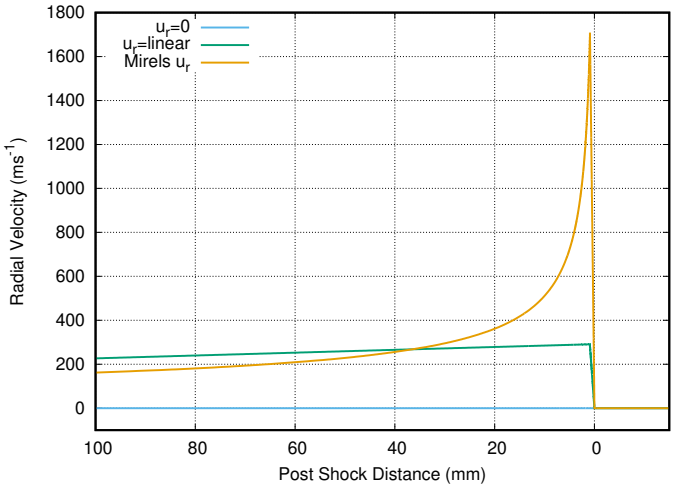

Fig. 5 The choice of the radial velocity profiles allows different models to be evaluated. $u_r = 0$ corresponds to Rankine-Hugoniot model, a linearly decreasing u_r corresponds to a blunt body sphere model and the Mirels u_r is relevant for shock tubes.

The radiance data is obtained as a function of post-shock distance, and focuses on the wavelength corresponding to the Oxygen 777nm triplet by integrating the radiance from 770-785nm. The results from use of the various radial velocity profiles are shown in Figure 6a. As the Mirels model incorporates mass loss to the boundary layer, the post shock time of flight is increased [19]. This results in the normal shock results and blunt body model having stretched radiance profiles as chemical equilibrium is not reached by 100mm post shock. This effect is most important further away from the shock, as the discrepancy in the particle time of flight increases due to it being proportional to the integral of $1/u$. As the Mirels profile is the most appropriate for shock tube flows due to the correction for the boundary layer growth present in shock tubes [21], it will be the profile used in subsequent analyses.

Figure 6b compares the performance of the NESS-NEQAIR generated radiance against POSHAX3-NEQAIR and LASTA-NEQAIR numerical codes. Although consistently underpredicting the radiance by a third throughout the observed region, NESS captures both the thermochemical non-equilibrium region up to 25mm compared to POSHAX, as well as capturing the shape of the chemical non-equilibrium region from approximately 25mm to 100mm. In comparison, POSHAX3-NEQAIR overpredicts the non-equilibrium peak and settles to the equilibrium value much faster than NESS-NEQAIR. This discrepancy is likely due to POSHAX not resolving shock structure. POSHAX3 relaxes the problem from a frozen post-shock state, increasing the rate of reactions towards equilibrium and thus resulting in increased radiance levels in the non-equilibrium region. Additionally, as a consequence of only considering the problem as a post-shock relaxation model, the equilibrium post shock state is constant. In comparison, NESS captures the compression effects due to the use of the Mirels profile, reproducing the curvature in the equilibrium region.

The result from LASTA contains both Mirels effects and shock history effects, but as it is an equilibrium solver the effects of chemical non-equilibrium predicted by NESS cannot be resolved. However, LASTA accounts for shock history effects while NESS does not, therefore as LASTA-NEQAIR predicts an increase in radiance through the test slug it is likely the NESS-NEQAIR results underpredict radiance from 40 mm onwards.

B. T6 Tunnel Low Earth Orbit Return Experiments

The second group of test cases considered in this paper were gathered during a campaign using the T6 tunnel in aluminium shock tube (AST) mode, designed to examine radiation experienced during the descent of vehicles from Low-Earth Orbit [12]. Test cases ranging from 5.5-7.2 km/s at a nominal post-shock pressure of 1 bar in synthetic air (20.78% O_2 and 79.22% N_2 by volume) produced radiance data in the UV/Vis and Vis/NIR spectral ranges. Table 1 details the summary of conditions chosen for analysis by NESS, with the shock velocity at the window used for the

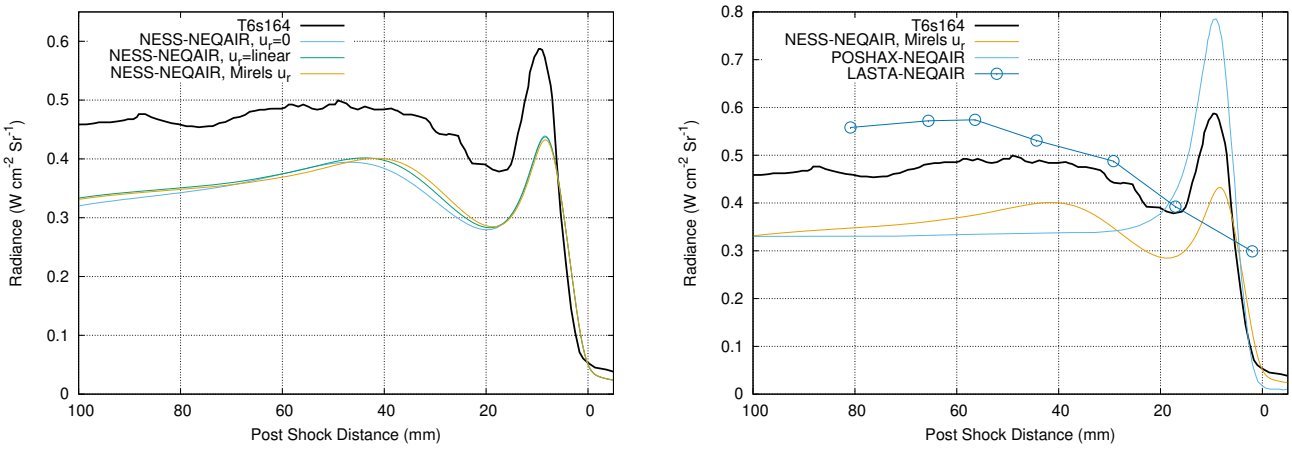

a) Comparison of the various radial velocity profiles

b) Comparison to POSHAX3 and LASTA

Fig. 6 Comparison of NESS results against T6s164 experimental results of a 9.59km/s shock in fill gas at 300K, 13.3 Pa, and composition of 79% N_2, 21% O_2 by volume.

simulations.

Table 1 T6 shot conditions chosen for analysis from Glenn et al. [12]

Shot no.	P_{fill} (Pa)	v_{shock}	$P_{2,Meas}$(kPa)
195	290.0	5.54	99
198	213.9	6.55	103
220	175.0	7.12	101

Radiance profiles have been generated numerically for comparison against T6 experimental data by feeding the temperatures and number densities predicted by NESS into NEQAIR v15.1, for wavelength regions 210-440nm in the UV/Vis and 600-840nm in the Vis/NIR. Spatial convolutions have been performed on the resulting numerical data, to enable a like-for-like comparison with the experimental radiance profiles. The spatial resolution function (SRF) used for these convolutions consists of three components, as detailed by Cruden [41]. The first component is smearing due to the resolution of the camera CCD arrays, which has been characterised experimentally via measurements of the point spread functions of each camera. The second component is due to the optics. Ray tracing analyses have been performed for each telescopic optical set up, to predict this function at the spatial location of the shock wave during the camera gating. Finally, the smearing due to motion of the shock is either approximated as a square pulse with width equal to the distance the shock travels during the camera gating, or if known, the camera gating function is used.

The radiance profiles for shot 195 are displayed in Figure 7, while data for shot 198 and 220 are included in Figures 8 and 9. Although the peak radiance predicted by NESS-NEQAIR is lower than experimental results, the shape of the rise is similar to the experimental results and equilibrium is reached at a similar distance. The peak radiance is larger in all cases except the Vis/NIR wavelength region in shot 220.

The radiation results of NESS are vastly different to the results predicted by the two temperature, Park 1990 POSHAX3 simulation conducted by Glenn et al [12], particularly for the 5.54 km/s shot 195 case. This discrepancy is likely due to POSHAX not resolving shock structure. POSHAX3 relaxes the problem from a frozen post-shock state, which increase the rate of reactions towards equilibrium. This results in lower radiance in the non-equilibrium region, suggesting that resolving shock structure is important when considering non-equilibrium radiance. In comparison, NESS resolves the shock producing a lower peak temperature and but allows reactions to occur inside the shock structure.

The results of NESS and POSHAX3 mostly converge to the same equilibrium value by approximately 30mm post-shock, but well below the experimental value. However, discrepancies between NESS-NEQAIR, POSHAX3-NEQAIR and LASTA-NEQAIR in the equilibrium of the UV/Vis wavelengths indicate sensitivity to small changes in temperatures and reaction rates chosen. Following Glenn et al., this is possibly due to the exclusion of the boundary layer radiation in

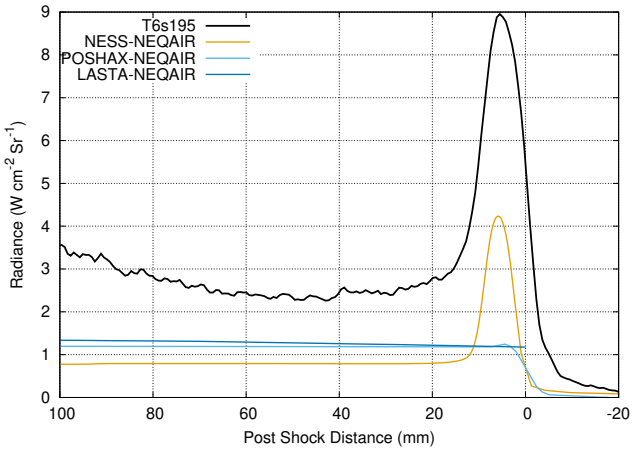

a) UV/Vis region (210-440 nm)

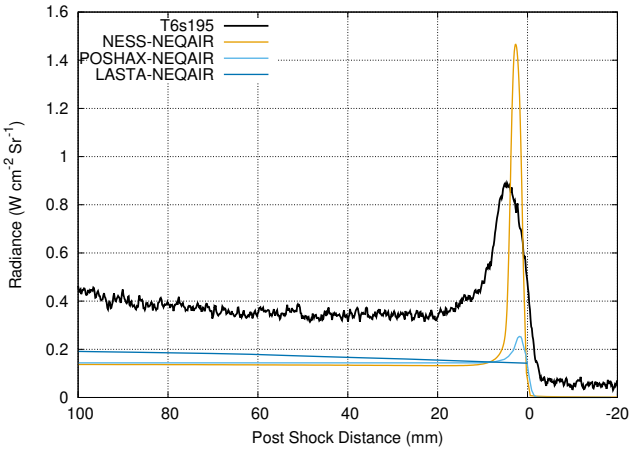

b) Vis/NIR region (600-840 nm)

Fig. 7 Results from shot 195, 5.54 km/s shock speed through a fill gas at 290 Pa, 300K, and composition of 79% N_2, 21% O_2 by volume. Absolute radiance is plotted as a function of post shock distance.

the analysis of NESS and POSHAX3, low level contamination, and the radiative modelling errors present in NEQAIR for molecular band radiation [12]. Glenn et al. also indicated that shock history effects were important and could account for some of the rise in radiance at the rear of the test slub through investigation using the equilibrium shock tube code LASTA [12]. Figures 7, 8 and 9 show LASTA-NEQAIR slightly increasing radiance towards the end of the viewing window, however the large rises present in shot 195 indicate that other contaminants may be present.

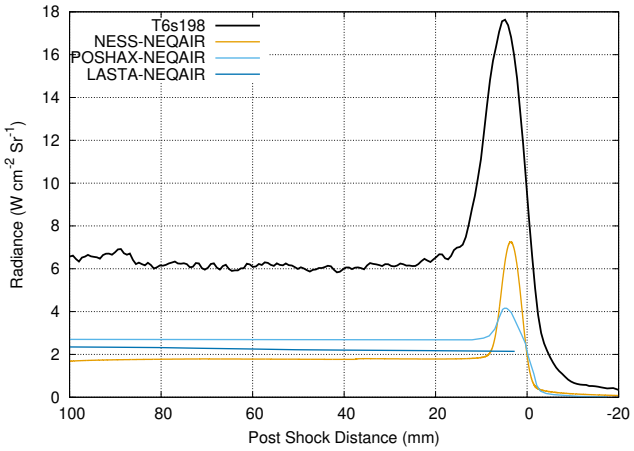

a) UV/Vis region (210-440 nm)

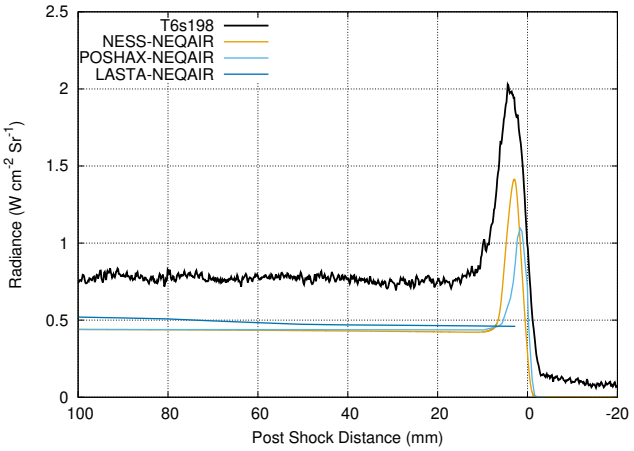

b) Vis/NIR region (600-840 nm)

Fig. 8 Absolute radiance as a function of position obtained in the T6 facility from shot 198, a 6.55 km/s shock through 213.9 Pa, 300K fill gas with composition of 79% N_2, 21% O_2 by volume.

Previous works by Cruden et al. [11, 42, 43] have used non-equilibrium metrics (NEMs) to analyse the non-equilibrium region of radiance profiles. This metric is designed to allow comparison of a simulations and experimental results and to minimise the effect of chosen SRF and ILS functions. The absolute NEM is the integrated radiance of the spectral radiance L (W cm^{-2} sr^{-1} μm^{-1}) over the spectral range and specified distance either side of peak radiance, commonly ±20 mm is used (see Equation 16).

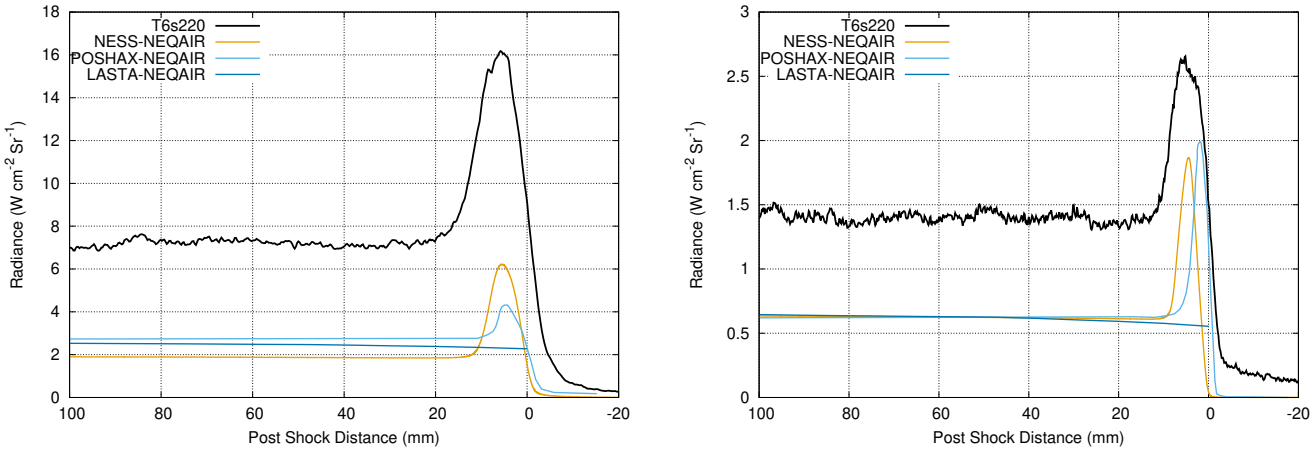

a) Vis/NIR region (210-440 nm) b) Vis/NIR region (600-840 nm)

Fig. 9 Results from shot 220, 7.12 km/s shock speed through a fill gas at 175 Pa, 300K, and composition of 79% N_2, 21% O_2 by volume. Absolute radiance is plotted as a function of post shock distance.

$$NEM_{\text{abs}} = \frac{1}{D_{\text{tube}}} \int_{\lambda_{\text{low}}}^{\lambda_{\text{high}}} \int_{y_{\text{pk}-\delta}}^{y_{\text{pk}+\delta}} L(y,\lambda)\, dy\, d\lambda \tag{16}$$

The NEMs for shots 195, 198 and 220 were calculated using both the normal $y_{\text{pk}} \pm 20$ mm and $y_{\text{pk}} \pm 10$ mm. The additional analysis using δ equal to 10 mm was made to minimise the differences in plateau radiance to give a more direct comparison of the non-equilibrium region.

The absolute NEM values for the three experiments are plotted in Figures 10 and 11 for the wavelength ranges 210-440 nm and 600-840 nm respectively. These results are compared directly against POSHAX3-NEQAIR and NESS-NEQAIR simulations. NESS-NEQAIR performs considerably better than POSHAX3-NEQAIR, particularly for 5.54 km/s in both wavelength regions. This is more evident by using $\delta = 10$ mm either side of the peak, indicating that NESS-NEQAIR produced relatively similar non-equilibrium results when the discrepancies in the equilibrium radiance are minimised. The NEM was doubled in both wavelength regions using $\delta = 10$ mm for the 5.54 km/s shock speed, and would have been significantly more than the POSHAX3-NEQAIR value in the 6.55 km/s if the equilibrium radiance was equal.

C. T6 and NASA-EAST Low Earth Orbit Return Experiments

Two comparable low Earth orbit return experiments are the T6 AST shot T6s207 from Glenn et al. [12] and NASA-EAST shot ES-59/47 (data available from the online repository). T6s207 was a nominally 6.64 km/s shock speed in 106.7 Pa synthetic air (20.78% O_2 and 79.22% N_2 by volume), while ES-59/47 was nominally 6.81 km/s shock through 94.13 Pa synthetic air (20.78% O_2 and 79.22% N_2 by volume).

Both of these shots produced radiance data in the UV/Vis and Vis/NIR spectral ranges, and appropriately convolved simulations from NESS-NEQAIR and LASTA-NEQAIR of these experiments are shown in Figures 12 and 13.

As in the last section, NESS produces results which are proportionally much smaller than the experimental values in both the equilibrium and non-equilibrium regions. However, the shape of the rise and fall of radiance matches well with the experimental results, and the offset seen between the equilibrium values found in the work of Glenn et al. [12] is also present in the EAST results. This indicates that some factors such as the exclusion of the boundary layer radiation in the analysis of NESS and LASTA or low level contamination may also be influencing the results from EAST. LASTA appropriately predicts the slope of the rise in radiance in each of the cases apart from the VUV results of T6s207, indicating contaminants may be influencing the increase in radiance in this region. The rise in equilibrium radiance of the EAST case exceeds that of NESS, which is expected due to shock deceleration down the tube increasing the temperature more than just by consideration of the boundary layer effects [17].

The experimental NEM values (using δ=20mm) of the two experiments are comparable in the 600-840 nm wavelength

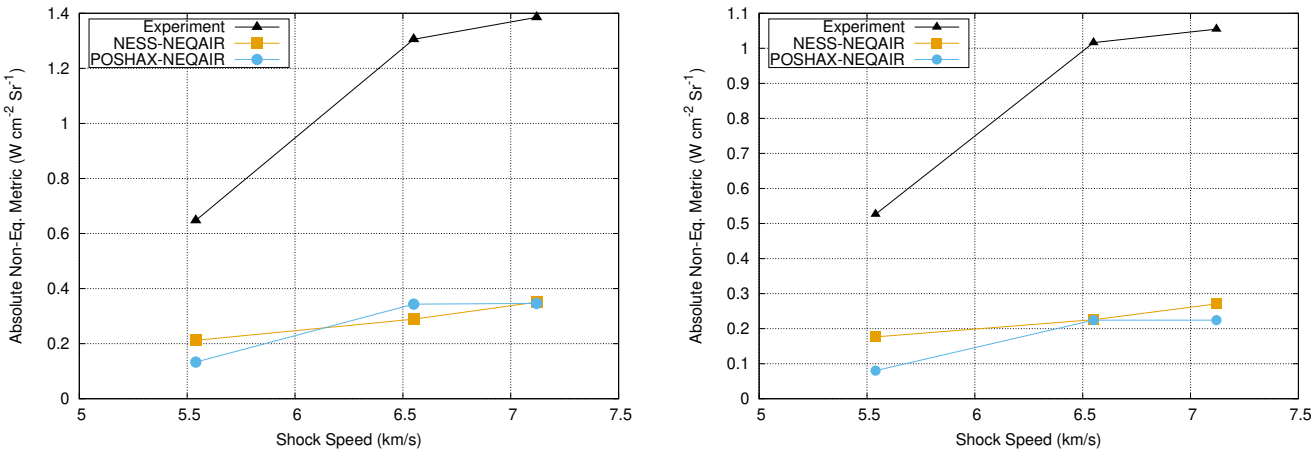

Fig. 10 Absolute non-equilibrium metric (NEM) values in the 210-440 nm region using δ equal to (a) 20 mm and (b) 10 mm.

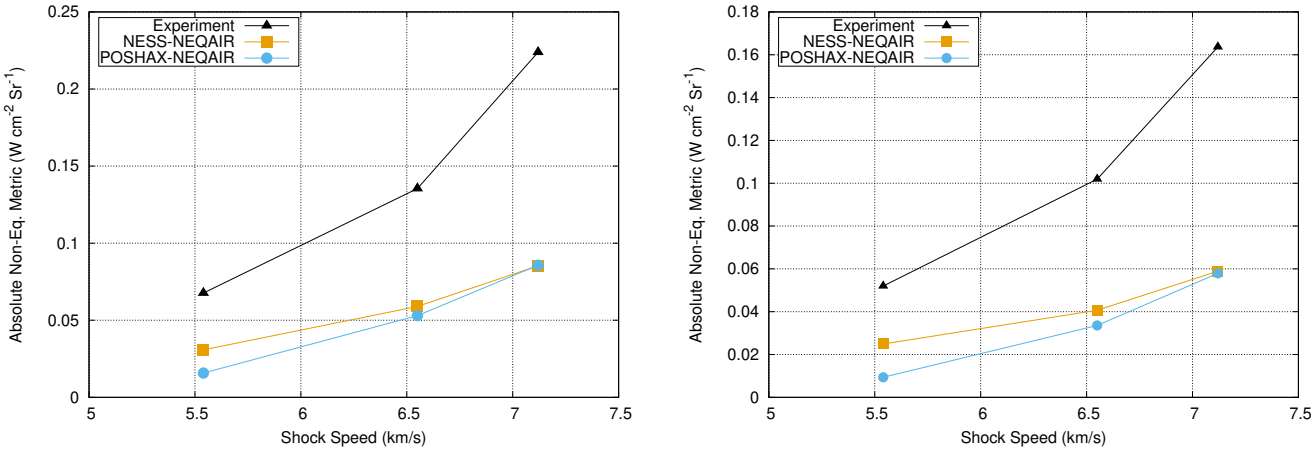

Fig. 11 Absolute non-equilibrium metric (NEM) values in the 600-840 nm region using δ equal to (a) 20 mm and (b) 10 mm.

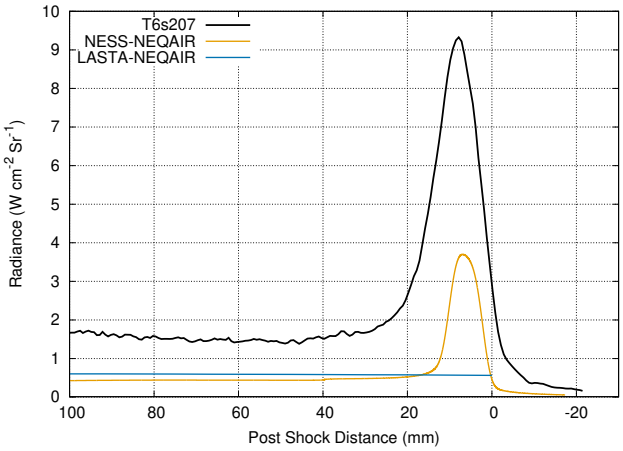

a) UV/Vis region (210-400 nm)

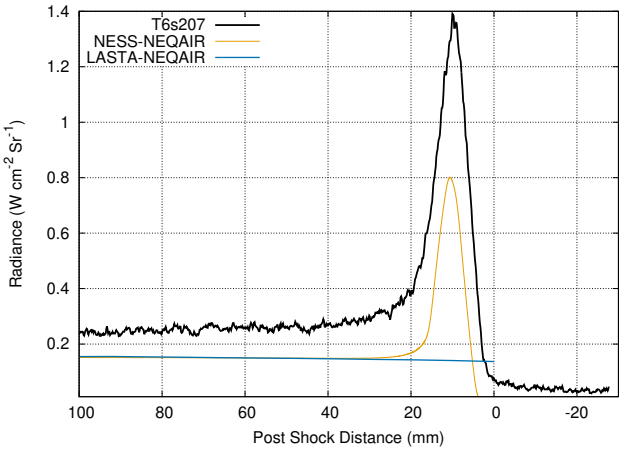

b) Vis/NIR region (600-840 nm)

Fig. 12 Absolute radiance as a function of position obtained in the T6 facility from shot 207, a 6.64 km/s shock through 106.7 Pa, 300K fill gas with composition of 79% N_2, 21% O_2 by volume.

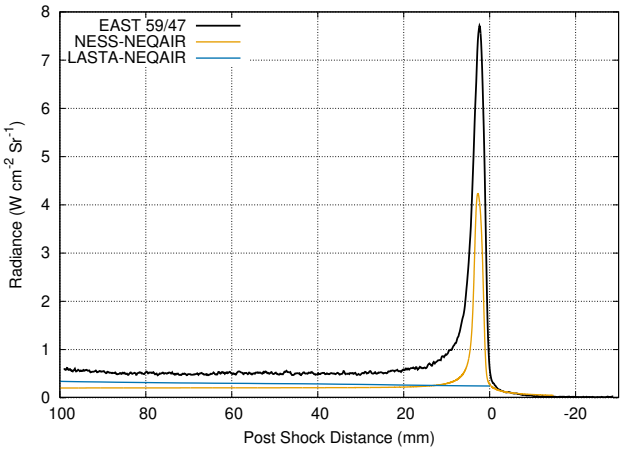

a) UV/Vis region (210-400 nm)

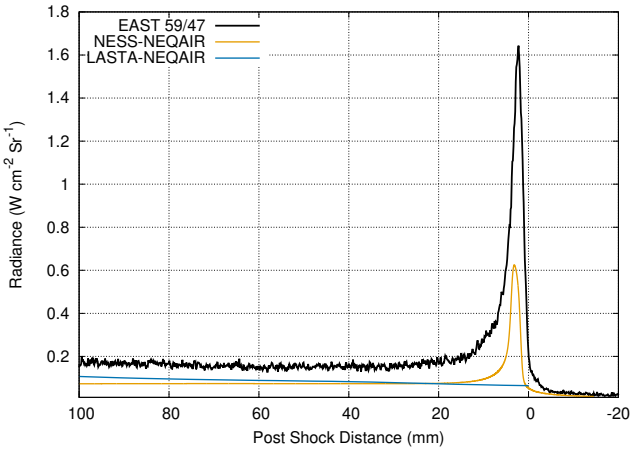

b) Vis/NIR region (600-840 nm)

Fig. 13 Absolute radiance as a function of position obtained in the NASA-EAST facility from shot 59/47, a 6.81 km/s shock through 94.13 Pa, 300K fill gas with composition of 79% N_2, 21% O_2 by volume.

region (15% difference), however there is an increase of radiance in the non-equilibrium region for the T6 data. The NEMs are shown in Table 2. The NEM results from NESS-NEQAIR are approximately a third of the values from the EAST experiment, and a quarter of the values from T6s207.

Table 2 Non-equilibrium metric results for T6s207 and ES-59/47.

Shot no.	Exp. 210-400 nm	NESS 210-400 nm	600-840 nm	NESS 600-840 nm
207	0.677	0.189	0.08316	0.0372
59/47	0.406	0.173	0.101	0.036

D. NASA EAST Experiments for Titan Entry

Reaction rates relevant for simulation of Titan entry are of interest to better understand heat flux loads entry vehicles may encounter [37]. Brandis and Cruden [37] examined data from a wide ranging experimental campaign targeting various points on a potential entry trajectory. One such experiment was shot T-61/19, a 6.1 km/s shock through 13.3 Pa, 300 K fill gas composed of 2% CH_4 and 98% N_2 by volume. The results from the experiment, NESS-NEQAIR simulations, along with simulations from NASA's DPLR codes are shown in 14. It is important to note that the DPLR code used for these simulations is a 3m radius blunt body sphere test case, under the assumption of a blunt body stagnation line analogy to the shock tube. However, recent work by Clarke et al. [19] demonstrates that the time of flight for the blunt body sphere will be vastly different compared to shock tube flow. This is due to the rapid growth of the boundary layer in the immediate post shock region, slowing the core flow down and subsequently increasing the time of flight of the flow. Clarke et al. found a spatial transformation to take simulations of a sphere stagnation line and transform them to coordinates relevant for shock tubes. This is shown in 14 as the transformed DPLR-NEQAIR results.

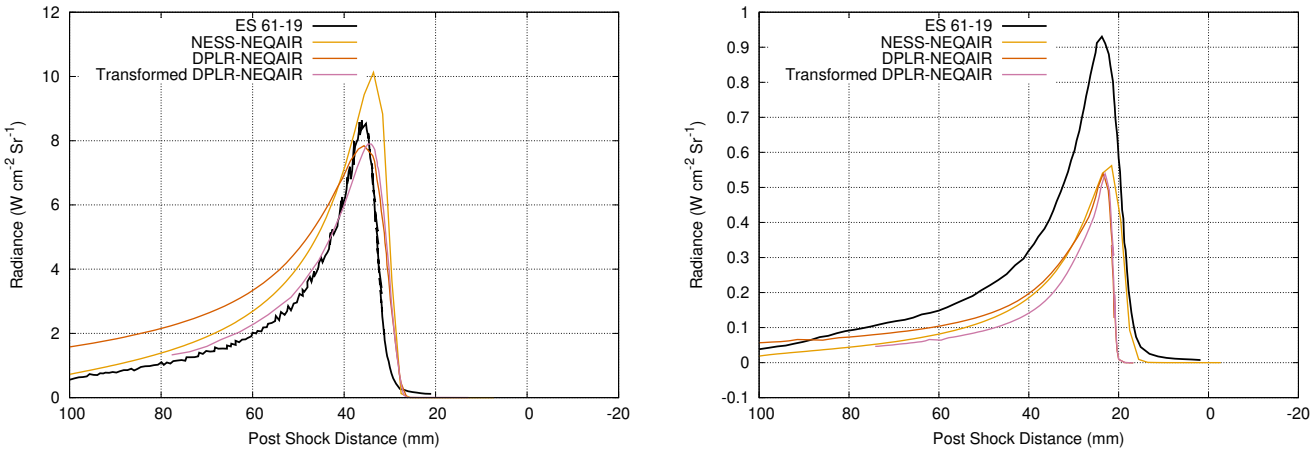

a) UV/Vis region (210-440 nm) b) Visible region (480-680 nm)

Fig. 14 Results from EAST shot T61/19, a 6.1 km/s shock speed through a fill gas at 13.3 Pa, 300K, and composition of 98% N_2, 2% CH_4 by volume. Absolute radiance is plotted as a function of post shock distance.

NESS-NEQAIR overpredicts the non-equilibrium peak by approximately 20% for the VUV region, but accurately captures the decay of radiance behind the peak. Similarly, although the peak value is lower than experimental results in the visible region, it is 4% larger than the DPLR-NEQAIR peak. The NESS-NEQAIR result also has a more similar decay in radiance compared to the experiment than the DPLR-NEQAIR results. These results demonstrate the importance of including boundary effects present in a shock tube. The relatively slow reaction rates found when analysing N_2-CH_4 gas mixtures results in time of flight effects becoming increasingly significant, and therefore modelling of Titan shock tube experiment must appropriately consider the unique flow dynamics present.

VII. Conclusions

An efficient method has been presented for calculating the non-equilibrium properties of a test gas in a shock tube. The method is based on a version of the parabolised Navier-Stokes equations formally similar to a stagnation line problem coupled with Park's two temperature model. The transport properties of the non-equilibrium gas are obtained using second order Chapman-Enskog theory. The effect of an artificial boundary layer is considered by coupling the model to a radial pressure function. Thus, this work examines the effect of shock structure and effective boundary layer for a non-equilibrium flow within a shock tunnel. Simulations requiring less than 5 minutes of run time enabled simulation of various air cases from Oxford's T6 Stalker tunnel and NASA EAST. These simulations demonstrated the improved performance of NESS compared to POSHAX3 for use in modelling high speed non-equilibrium flows. The resolution of shock structure and chosen reaction rate model improved agreement between simulations and experiments for air cases ranging from 5.5km/s to 9.54 km/s.

Modelling of a 6.1 km/s, 13.3 Pa NASA-EAST shock tube experiment relevant to Titan entry demonstrated the importance of using appropriate flow solvers for modelling shock tube flows. The difference in time of flight for a blunt body stagnation line is significant compared to a numerical model which accounts for the rapid growth of the boundary layer in shock tubes. For flows relevant to Titan where radiating species have slower reaction rates, this becomes increasingly important. The developed method appropriately modelled the peak and subsequent decay in radiance in the post shock region. Further development of the algorithm to include shock trajectory effects and a self-similar boundary layer will extend the applicability of the model. This model can then be utilised in a variety of ways, including for new analysis of rate-coefficients as well as sensitivity calculations of the results.

References

[1] Park, C., *Nonequilibrium Hypersonic Aerothermodynamics*, Wiley, New York, 1990.

[2] McGilvray, M., Doherty, L., Morgan, R., and Gildfind, D., "T6: The Oxford University Stalker Tunnel," *20th AIAA International Space Planes and Hypersonic Systems and Technologies Conference*, AIAA, Washington, DC, 2015, pp. 1–11. https://doi.org/10.2514/6.2015-3545.

[3] Freedman, E., and Daiber, J. W., "Decomposition Rate of Nitric Oxide Between 3000 and 4300°K," *The Journal of Chemical Physics*, Vol. 34, No. 4, 1961, pp. 1271–1278. https://doi.org/10.1063/1.1731731.

[4] Dunn, M. G., and Lordi, J. A., "Measurement of $O_2^+ + e^-$ Dissociative Recombination in Expanding Oxygen Flows," *AIAA Journal*, Vol. 8, No. 4, 1970, pp. 614–618. https://doi.org/10.2514/3.5730.

[5] Byron, S., *Interferometric Measurement in a Shock Tube of Dissociation Rates for Air and its Component Gases*, Cornell University, New York, 1959.

[6] Park, C., "Two-temperature interpretation of dissociation rate data for N_2 and O_2," *26th Aerospace Sciences Meeting*, American Institute of Aeronautics and Astronautics, 1988. https://doi.org/10.2514/6.1988-458, URL https://arc.aiaa.org/doi/10.2514/6.1988-458.

[7] Park, C., "Assessment of a Two-Temperature Kinetic Model for Dissociating and Weakly Ionizing Nitrogen," *Journal of Thermophysics and Heat Transfer*, Vol. 2, No. 1, 1988, pp. 8–16. https://doi.org/10.2514/3.55.

[8] Satchell, M., Glenn, A., Collen, P., Penty-Geraets, R., McGilvray, M., and di Mare, L., "Analytical Method of Evaluating Nonuniformities in Shock Tube Flows: Application," *AIAA Journal*, Vol. 60, No. 2, 2022, pp. 669–676. https://doi.org/10.2514/1.J060991.

[9] Dann, A. G., Morgan, R. G., Gildfind, D. E., Jacobs, P. A., McGilvray, M., and Zander, F., "Upgrade of the X3 Super-Orbital Expansion Tube," *Proceedings of the 18th Australasian Fluid Mechanics Conference, AFMC 2012*, 2012, pp. 3–6.

[10] Brandis, A. M., Johnston, C. O., and Cruden, B. A., "Nonequilibrium Radiation for Earth Entry," *AIAA Paper 2016–3690*, June 2016. https://doi.org/10.2514/6.2016-3690.

[11] Cruden, B. A., "Radiance measurements for low density Mars entries," *43rd AIAA Thermophysics Conference 2012*, American Institute of Aeronautics and Astronautics, Reston, Virigina, 2012, pp. 3–6. https://doi.org/10.2514/6.2012-2742, URL https://arc.aiaa.org/doi/10.2514/6.2012-2742.

[12] Glenn, A. B., Collen, P. L., and McGilvray, M., "Experimental Non-Equilibrium Radiation Measurements for Low-Earth Orbit Return," *AIAA Science and Technology Forum and Exposition, AIAA SciTech Forum 2022*, 2022. https://doi.org/10.2514/6.2022-2154.

[13] Park, C., "Review of chemical-kinetic problems of future NASA missions, I: Earth entries," *Journal of Thermophysics and Heat Transfer*, Vol. 7, No. 3, 1993, pp. 385–398. https://doi.org/10.2514/3.431.

[14] Gnoffo, P. A., Gupta, R. N., and Shinn, J. L., "Conservation Equations and Physical Models for Hypersonic Air Flows in Thermal and Chemical Nonequilibrium," Tech. Rep. NASA-TP-2867, NASA, 1989.

[15] Satchell, M., McGilvray, M., and Di Mare, L., "Analytical Method of Evaluating Nonuniformities in Shock Tube Flows: Theory and Development," *AIAA Journal*, 2021, pp. 1–15. https://doi.org/10.2514/1.j060990.

[16] Satchell, M., di Mare, L., and McGilvray, M., "Flow Nonuniformities Behind Accelerating and Decelerating Shock Waves in Shock Tubes," *AIAA Journal*, Vol. 60, No. 3, 2022, pp. 1537–1548. https://doi.org/10.2514/1.J060375.

[17] Collen, P. L., Satchell, M., Di Mare, L., and McGilvray, M., "The influence of shock speed variation on radiation and thermochemistry experiments in shock tubes," *Journal of Fluid Mechanics*, Vol. 948, 2022, p. A51. https://doi.org/10.1017/jfm.2022.727.

[18] Clarke, J., Glenn, A., McGilvray, M., and di Mare, L., "Numerical Model for Non-Equilibrium Shock Tube Flow," *9th International Workshop on Radiation of High Temperature Gases for Space Missions*, 2022.

[19] Clarke, J., di Mare, L., and McGilvray, M., "Analysis of Shock Tube Data," , 2022.

[20] Mirels, H., "Test time in low-pressure shock tubes," *Physics of Fluids*, Vol. 6, No. 9, 1963, pp. 1201–1214. https://doi.org/10.1063/1.1706887.

[21] Mirels, H., "Flow nonuniformity in shock tubes operating at maximum test times," *Physics of Fluids*, Vol. 9, No. 10, 1966, pp. 1907–1912. https://doi.org/10.1063/1.1761542.

[22] Gupta, R. N., Yos, J. M., Thompson, R. A., and Lee, K.-P., "A Review of Reaction Rates and Thermodynamic and Transport Properties for an 11 Species Air Model for Chemical and Thermal Nonequilibrium Calculations to 30 000 K," Tech. Rep. NASA-RP-1232, NASA, 1990.

[23] Moss, J. N., "Reacting Viscous-Shock-Layer Solutions with Multicomponent Diffusion and Mass Injection," Tech. Rep. NASA-TR-R-411, NASA, 1974.

[24] Lee, J.-H., "Basic Governing Equations for the Flight Regimes of Aeroassisted Orbital Transfer Vehicles," *19th Thermophysics Conference*, American Institute of Aeronautics and Astronautics, Reston, Virigina, 1984. https://doi.org/10.2514/6.1984-1729, URL https://arc.aiaa.org/doi/10.2514/6.1984-1729.

[25] Lee, J.-H., "Electron-Impact Vibrational Excitation Rates in the Flowfield of Aeroassisted Orbital Transfer Vehicles." *Progress in Astronautics and Aeronautics*, Vol. 103, 1986, pp. 197–224. https://doi.org/10.2514/5.9781600865770.0197.0224.

[26] Millikan, R. C., and White, D. R., "Systematics of vibrational relaxation," *The Journal of Chemical Physics*, Vol. 39, No. 12, 1963, pp. 3209–3213. https://doi.org/10.1063/1.1734182.

[27] Park, C., "Problems of Rate Chemistry in the Flight Regimes," *AIAA 19th Thermophysics Conference*, 1984, pp. 1–11.

[28] Dunn, M. G., and Kang, S. W., "Theoretical and Experimental Studies of Reentry Plasmas." *NASA Contractor Reports*, , No. April, 1973.

[29] Morduchow, M., and Libby, P. A., "On a Complete Solution of the One-Dimensional Flow Equations of a Viscous, Heat-Conducting, Compressible Gas," *Journal of the Aeronautical Sciences*, Vol. 16, No. 11, 1949, pp. 674–684. https://doi.org/10.2514/8.11882.

[30] Potter, D. F., "Modelling of radiating shock layers for atmospheric entry at Earth and Mars," Ph.D. thesis, University of Queensland, 2011.

[31] Gollan, R. J., "The Computational Modelling of High-Temperature Gas Effects with Application to Hypersonic Flows," Ph.D. thesis, University of Queensland, 2008.

[32] Marrone, P. V., and Treanor, C. E., "Chemical relaxation with preferential dissociation from excited vibrational levels," *Physics of Fluids*, Vol. 6, No. 9, 1963, pp. 1215–1221. https://doi.org/10.1063/1.1706888.

[33] Collen, P., Doherty, L. J., Subiah, S. D., Sopek, T., Jahn, I., Gildfind, D., Penty Geraets, R., Gollan, R., Hambidge, C., Morgan, R., and McGilvray, M., "Development and commissioning of the T6 Stalker Tunnel," *Experiments in Fluids*, Vol. 62, No. 11, 2021, p. 225. https://doi.org/10.1007/s00348-021-03298-1, URL https://link.springer.com/10.1007/s00348-021-03298-1.

[34] Collen, P. L., Di Mare, L., McGilvray, M., and Satchell, M., "Analysis of Shock Deceleration Effects on Radiation Experiments in the NASA Electric Arc Shock Tube." *AIAA Science and Technology Forum and Exposition, AIAA SciTech Forum 2022*, 2022. https://doi.org/10.2514/6.2022-0267.

[35] Cruden, B. A., "Absolute Radiation Measurements in Earth and Mars Entry Conditions," Tech. Rep. STO AVT-218-VKI, NATO, 2014.

[36] Whiting, E. E., Chul, P., Liu, Y., Arnold, O., and Paterson, A., "NEQAIR96, Nonequilibrium and Equilibrium Radiative Transport and Spectra Program: User's Manual," Tech. Rep. December, NASA, 1996.

[37] Brandis, A. M., and Cruden, B. A., "Titan atmospheric entry radiative heating," *47th AIAA Thermophysics Conference, 2017*, 2017, pp. 1–27. https://doi.org/10.2514/6.2017-4534.

[38] Kim, J. G., "Expansion of the equilibrium constants for the temperature range of 300K to 20,000K," *International Journal of Aeronautical and Space Sciences*, Vol. 17, No. 4, 2016, pp. 455–466. https://doi.org/10.5139/IJASS.2016.17.4.455.

[39] McBride, B. J., Zehe, M. J., and Gordon, S., "NASA Glenn coeefficients for calculating thermodynamic properties of individual species," , No. September, 2002.

[40] André, P., Aubreton, J., Clain, S., Dudeck, M., Duffour, E., Elchinger, M. F., Izrar, B., Rochette, D., Touzani, R., and Vacher, D., "Transport coefficients in thermal plasma. Applications to Mars and Titan atmospheres," *European Physical Journal D*, Vol. 57, No. 2, 2010, pp. 227–234. https://doi.org/10.1140/epjd/e2010-00036-5.

[41] Cruden, B. A., "Absolute radiation measurements in earth and mars entry conditions," *NATO RTO Lecture Series RTO-EN-AVT-218*, 2014.

[42] Brandis, A., Johnston, C., Cruden, B., and Prabhu, D., "Investigation of Nonequilibrium Radiation for Mars Entry," *51st AIAA Aerospace Sciences Meeting including the New Horizons Forum and Aerospace Exposition*, American Institute of Aeronautics and Astronautics, Reston, Virigina, 2013, pp. 1–36. https://doi.org/10.2514/6.2013-1055, URL https://arc.aiaa.org/doi/10.2514/6.2013-1055.

[43] Cruden, B. A., and Brandis, A. M., "Measurement of Radiative Non-equilibrium for Air Shocks Between 7-9 km/s," *47th AIAA Thermophysics Conference*, American Institute of Aeronautics and Astronautics, Reston, Virginia, 2017, pp. 1–36. https://doi.org/10.2514/6.2017-4535, URL https://arc.aiaa.org/doi/10.2514/6.2017-4535.